Review of Scientific Instruments

CR-39 nuclear track detector response to inertial confinement fusion relevant ions

Cite as: Rev. Sci. Instrum. **91**, 053502 (2020); https://doi.org/10.1063/5.0004129
Submitted: 07 February 2020 . Accepted: 23 April 2020 . Published Online: 13 May 2020

B. Lahmann, M. Gatu Johnson, J. A. Frenje, Y. Yu. Glebov, H. G. Rinderknecht, F. H. Séguin, G. Sutcliffe, and R. D. Petrasso

Review of Scientific Instruments ARTICLE scitation.org/journal/rsi

CR-39 nuclear track detector response to inertial confinement fusion relevant ions

Cite as: Rev. Sci. Instrum. 91, 053502 (2020); doi: 10.1063/5.0004129
Submitted: 7 February 2020 • Accepted: 23 April 2020 •
Published Online: 13 May 2020

B. Lahmann,[1,a)] M. Gatu Johnson,[1] J. A. Frenje,[1] Y. Yu. Glebov,[2] H. G. Rinderknecht,[2] F. H. Séguin,[1] G. Sutcliffe,[1] and R. D. Petrasso[1]

AFFILIATIONS

[1] Massachusetts Institute of Technology, Cambridge, Massachusetts 02139, USA
[2] University of Rochester Laboratory For Laser Energetics, Rochester, New York 14623, USA

[a)] **Author to whom correspondence should be addressed:** lahmann@mit.edu

ABSTRACT

The detection properties of CR-39 were investigated for protons, deuterons, and tritons of various energies. Two models for the relationship between the track diameter and particle energy are presented and demonstrated to match experimental data for all three species. Data demonstrate that CR-39 has 100% efficiency for protons between 1 MeV and 4 MeV, deuterons between 1 MeV and 12.2 MeV, and tritons between 1 MeV and 10 MeV. The true upper bounds for deuterons and tritons exceed what could be measured in data. Simulations were developed to further explore the properties of CR-39 and suggest that the diameter–energy relationship of alpha particles cannot be captured by the conventional c-parameter model. These findings provide confidence in CR-39 track diameter based spectroscopy of all three species and provide invaluable insight for designing filtering for all CR-39 based diagnostics.

I. INTRODUCTION

The field of inertial confinement fusion (ICF) has relied heavily on solid-state nuclear track detectors made from CR-39 for several decades to provide counting, spectroscopy, and imaging of both neutrons and charged particles.[1–22] This is due, in part, to CR-39's complete insensitivity to electromagnetic pulses (EMPs) and near-complete insensitivity to x rays,[23,24] both of which are widely present in these environments. Additionally, CR-39 detectors have 100% detection efficiency for ions over wide energy ranges.[5]

While diagnostics based on CR-39 detectors such as the magnetic recoil spectrometers (MRSs),[8] charged particle spectrometers (CPSs),[5] and wedge range filters (WRFs)[5,12] all routinely measure multiple different charged particle species, most detailed response studies have been limited to neutron or proton measurements.[4,5,23,25–28] Recently, there has been much interest in experiments involving the T^3He fusion reaction,[5]

$$T + {}^3He \rightarrow \begin{cases} {}^4He + n + p + 12.1\ \text{MeV} \\ {}^4He\ (4.8\ \text{MeV}) + D\ (9.5\ \text{MeV}). \end{cases} \quad (1)$$

In particular, there has been interest in precise measurements of the 9.5 MeV deuteron in a variety of contexts. Examples include using them to characterize stellar-nuclear plasma platforms[29–31] and using them as a backlight to other experiments.[32] Additionally, there has been a recent renewed interest in the measurement of "knock-ons" from secondary reactions to measure and image fuel areal density in layered DT implosions.[33] These reactions are[5]

$$n\ (14.1\ \text{MeV}) + D \rightarrow n' + D\ (\leq 12.5\ \text{MeV}), \quad (2a)$$

$$n\ (14.1\ \text{MeV}) + T \rightarrow n' + T(\leq 10.6\ \text{MeV}). \quad (2b)$$

To accurately infer a spectrum from non-magnetic based CR-39 spectrometers such as the WRFs and step range filters (SRFs),[17] the analysis relies heavily on a detailed understanding of the CR-39 response. Currently, these detectors use response curves derived from proton data whenever the need arises.

For these reasons, documenting CR-39's response to charged particles (in particular, deuterons and tritons) is of great interest to the ICF community. A thorough understanding of the response provides additional confidence in both past and future measurements

and provides important information for detector configurations in future experiments.

II. CHARGED PARTICLE DETECTION WITH CR-39

CR-39 is a clear plastic material with the chemical composition $C_{12}H_{18}O_7$ and mass density roughly equal to 1.3 g/cm^3. When charged particles range through CR-39, they leave localized trails of damage in the material's molecular structure along the particle's path. If the CR-39 is subsequently etched in a bath of NaOH under specific conditions, the trails of damage will etch away significantly faster than the bulk material creating micrometer sized pits or "tracks" on the CR-39 surface.[5,34] So, as long as the bulk material is not etched beyond the end of this trail, the diameter of these tracks increases monotonically with the etch time (τ_E) and the local stopping power (dE/dx) of the particle. The dependence of dE/dx can be accurately modeled by the Bethe equation,[35]

$$\frac{dE}{dx} \propto \frac{Z^2 A}{E} \log\left(\tilde{I}\frac{E}{A}\right), \tag{3}$$

where E, Z, and A are the particle's energy, charge, and mass, respectively, and $\tilde{I}$ is a constant related to the ionization potential of CR-39. The log term (often referred to as the Column logarithm) is relatively constant at high energies (>0.5 MeV/amu) but changes rapidly for lower energies. This dependence is plotted in Fig. 1. Because of these dependencies, the resultant track diameters are also a function of the particle's mass and incident energy.

As seen in Fig. 1, dE/dx reaches a maximum and quickly plummets to zero at lower energies. This maximum results in an analogous maximum diameter ($D_{\max}$) that depends on the particle species

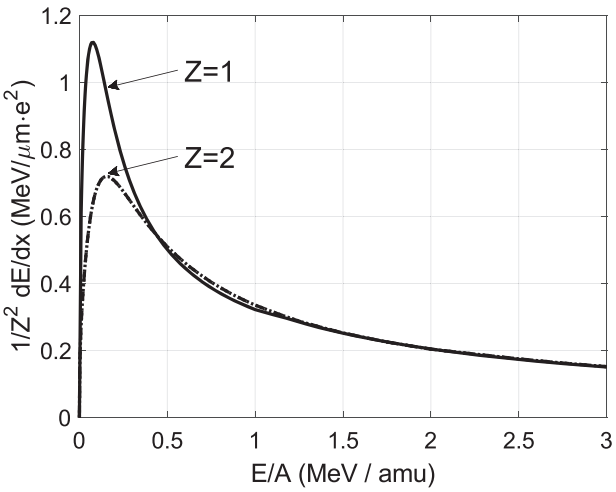

FIG. 1. Stopping power of particles in CR-39 as calculated by SRIM.[36] For sufficiently high energies, the stopping power depends only on the ratio E/Z^2A, and for a fixed Z, the entirety of the stopping power depends only on the ratio E/A.[35] At lower energies, the exact behavior of the stopping power depends on higher order terms of Z resulting in the deviations seen above.[37] When approaching from higher energies, the stopping power curves rapidly plummet after reaching a maximum (often referred to as the Bragg peak[38]).

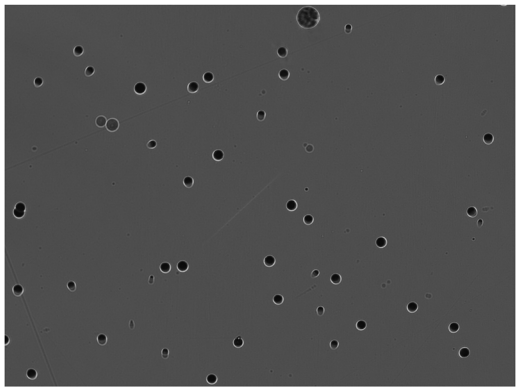

FIG. 2. Example microscope image from a piece of CR-39 exposed to 3.0 MeV protons from the MIT-HEDP Accelerator Facility.[39] Tracks vary in diameter and contrasts in accordance to the energy of the originating protons. Some small-faint tracks are intrinsic defects in the CR-39 that are ignored or subtracted in analysis. These data are from the accelerator shot named A2019121201.

and etch conditions of the CR-39. In practice, $D_{\max}$ serves as a useful reference point in several analyses, used specifically to scale and account for differences in τ_E and CR-39 properties. The energy at which $D_{\max}$ occurs [$E(D_{\max})$] is a few times higher than where dE/dx is maximized. This is because a particle will lose the entirety of its energy approximately when dE/dx is maximized, which, in turn, truncates the track development. The exact details of this energy and how it varies for different species are discussed in Sec. IV.

Tracks are ultimately measured using an optical microscope where they appear as darkened circles on the surface. This is because the CR-39 bulk surface is perpendicular to the backlight while the conical track surfaces are not leading to a relative decrease in transmission. An image of typical tracks is shown in Fig. 2. The amount of light transmitted is a function of the angle the track makes relative to the back-light.

III. DIAMETER–ENERGY RELATIONSHIP FOR IONS IN CR-39

The etching process that creates tracks can be modeled as radially isotropic etch-wave sources being created dynamically along the particle's path with some track-etch velocity $\vec{v}_T$. The etch waves travel outward at speed $|\vec{v}_B|$. The etching of the bulk material can be modeled as a plane wave source etching downward with the same speed $|\vec{v}_B|$.

As discussed in Sec. II, the track-etch velocity is a function of the local stopping power dE/dx of the charged particle and can be modeled as[40]

$$|\vec{v}_T(E)| = |\vec{v}_B|\left(1 + k\left(\left[\frac{dE}{dx}(E)\right]_{\frac{\text{keV}}{\mu\text{m}}}\right)^n\right), \tag{4}$$

where $\vec{v}_B$ is the bulk-etch velocity, k and n are empirical calibration constants to match observed data, and E is the energy the charged particle had when it crossed through the point being evaluated. The exact values of k and n vary with each piece of CR-39 due to difference in both the manufacturing and analysis processes. With this in

place, detailed track shapes can be simulated for a variety of particle species and energies. An example of this modeling is shown in Fig. 3.

With Eq. (4) and some simplifying assumptions, it can be shown that the track diameter relationship as a function of energy can be expressed as

$$D(E) \sim \frac{2\tau_E|\vec{v}_B|}{1 + k'(E_{\mathrm{MeV}}/Z^2A)^{n'}}, \tag{5}$$

where τ_E is the etch time, k' and n' are different empirical constants, E_{MeV} is the energy of the particle in MeV, Z is the charge, and A is the atomic mass number. This equation assumes that the Coulomb logarithm is relatively constant, which is sufficiently satisfied when the particle range is a few factors greater than the bulk-etch depth $\tau_E|\vec{v}_B|$. A more complete derivation is carried out in Appendix A. Hereafter, this equation will be referred to as the two-parameter model.

In practice, a much more complicated set of equations presented in Appendix B (hereafter referred to as the c-parameter model) is used for fitting proton data. It depends on a single fit parameter (c), as well as $D_{\max}$. Unlike the two-parameter model, the c-parameter model retains none of the mass and charge dependence from dE/dx. This makes the two-parameter model useful from a pedagogical standpoint because the effects of different species are easier to ascertain. $\tau_E|\vec{v}_B|$ is dictated entirely by the CR-39 etching process,

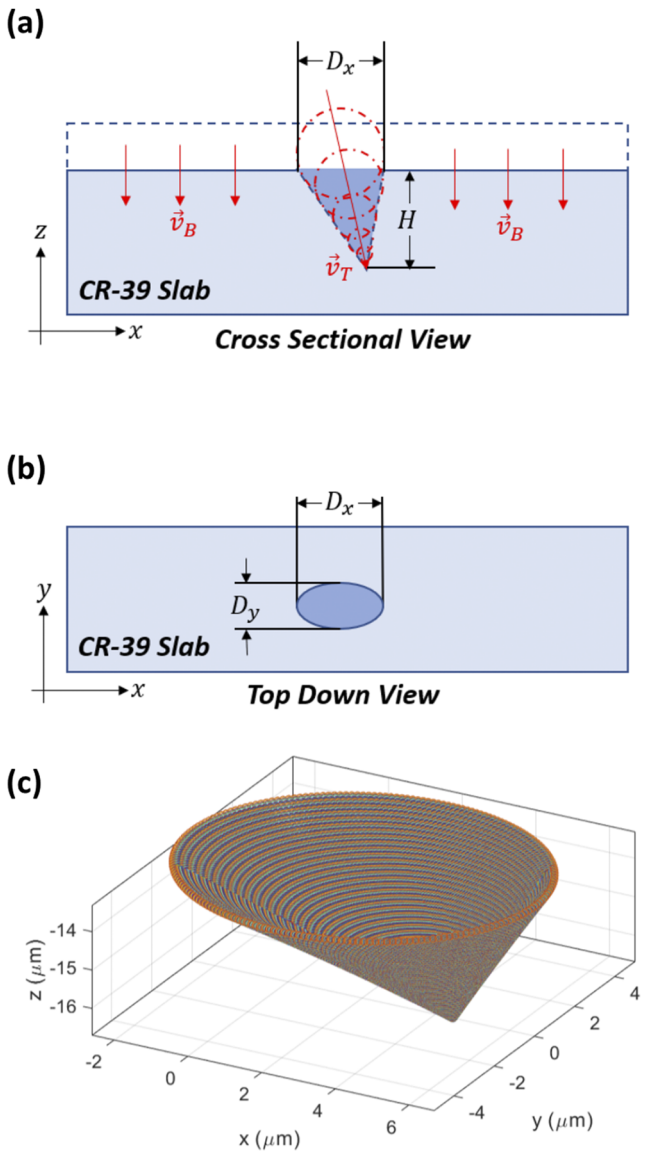

FIG. 3. Track evolution model used to simulate the characteristics of CR-39 tracks. Tracks are generated by a time evolving etch source that travels through the slab with velocity $\vec{v}_T(t)$ etching outward isotropically with velocity $\vec{v}_B$. Additionally, a bulk etch source is modeled as a plane wave traveling downward normal to the CR-39 surface with the same velocity $\vec{v}_B$. Figure 3(a) shows a cartoon of the cross-sectional view of a CR-39 slab, while Fig. 3(b) shows a top-down view (as would be seen by using a microscope). Figure 3(c) shows an example track generated from this model. The track was generated from a 2.0 MeV proton with a 15° incident angle relative to the surface normal. A τ_E = 5h etch was modeled using $|\vec{v}_B|$ = 2.66 μm/h, $k = 6 \times 10^{-5}$, and n = 2.76. This resulted in a track with diameters D_x = 9.30 μm and D_y = 8.42 μm and a depth (H) of 3.40 μm.

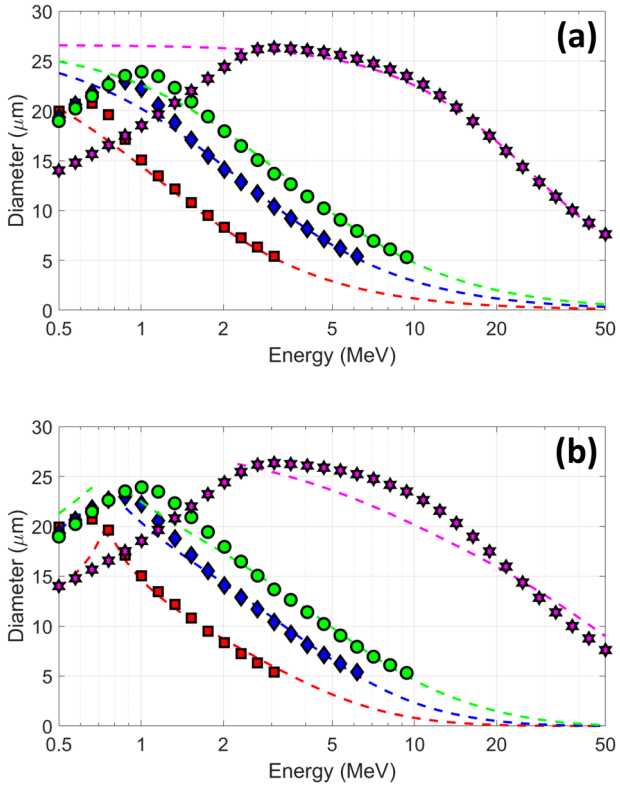

FIG. 4. Expected CR-39 track diameter vs energy for protons (red squares), deuterons (blue diamonds), tritons (green circles), and alphas (magenta stars). Square data points are the results from the model of the CR-39 etch process discussed in Sec. III, while the curves are fits. Figure 4(a) shows the two-parameter model fitted to the simulated data, and Fig. 4(b) shows the more standard c-parameter model fitted to the same simulated data. All of the data are generated using $|\vec{v}_B|$ = 2.66 μm/h, τ_E = 5 h, $k = 6 \times 10^{-5}$, and n = 2.76 from Eq. (4) to resemble typical experimental data. The fits in both Figs. 4(a) and 4(b) use values shown in Table I.

TABLE I. Diameter vs energy fit values to simulated data.

	Simple fit			c-Parameter fit	
Particle	$2\tau_E\lvert\vec{v}_B\rvert$ (μm)	k'	n'	$D_{\max}$ (μm)	c
p	26.6	0.7609	1.497	20.81	1.381
d	26.6	0.8389	1.415	22.98	1.020
t	26.6	0.8689	1.383	23.92	0.741
α	26.6	0.3938	1.676	26.35	0.146

and k' and n' are constant for a given piece of CR-39. The track diameter is, therefore, strictly a function of the ratio $E/(Z^2A)$. When compared to protons of the same energy, other particle species will have larger diameters due to the Z^2A increase in dE/dx. Figure 4 shows this simple equation for different species compared to the more rigorous model of the etch process discussed previously for various particles.

In Fig. 4, it is shown that both the two-parameter model and the c-parameter model work well for the simulated proton, deuteron, and triton data. In Table I, it is shown that the best-fit values for k' and n' are similar for these three particles because most of the differences in the diameter–energy relationships are well described by the ratio $E/(Z^2A)$. By contrast, while the c-parameter model works just as well, the best-fit c values drop significantly as the particle's mass increases.

While the two-parameter model does match the alpha-particle data, the best-fit values for k' and n' are significantly different when compared to the fits of the other three particle data. This is because terms of higher order than Z^2 are required to correctly describe the stopping power of alpha particles at these energies, and this is not accounted for in the derivation.[37] Presumably for the same reason, the c-parameter model fails to match the alpha data at all.

IV. ENERGY RANGE OF CHARGED PARTICLE DETECTION IN CR-39

As discussed in Sec. II, tracks are ultimately measured using an optical microscope system. Tracks are detectable when their angle is sufficiently steep to limit the transmission of the back-light as governed by the Fresnel equations. A single cartoon of this is shown in Fig. 5.

Using the model discussed in Sec. III, we can also investigate how this angle depends on energy and particle species. If $\vec{v}_T$ is constant, the depth of a track is simply proportional to the difference between the etch velocities,

$$H = \tau_E(|\vec{v}_T| - |\vec{v}_B|), \tag{6}$$

and the diameter is well approximated by Eq. (A5). Since $\vec{v}_T$ is constant, the resultant track would be conical, being defined by a single angle θ given by

$$\tan\theta = \frac{D}{2H} = \frac{|\vec{v}_B|}{|\vec{v}_T|}. \tag{7}$$

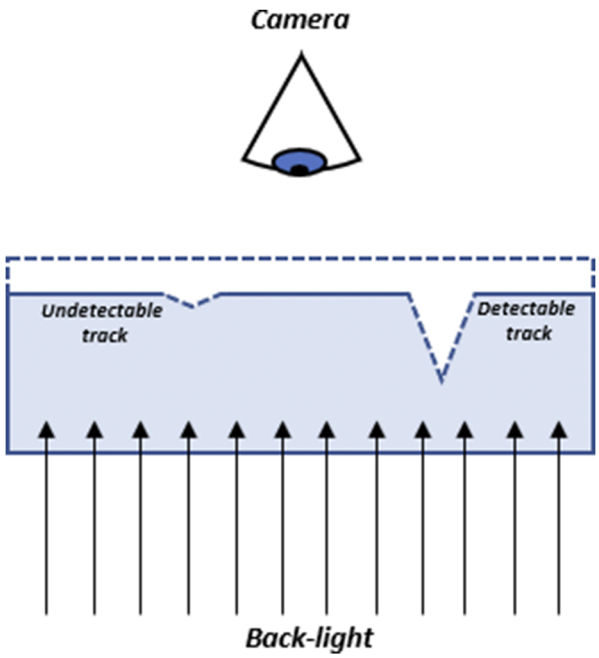

FIG. 5. Cartoon of a detectable and undetectable track in a piece of CR-39. Tracks are detected by using an optical microscope when the track's angle is sufficiently steep, so as to limit the transmission of the back-light. When tracks are too shallow, the back-light transmission through the track will be very similar to the transmission through the bulk medium, making it effectively invisible to the camera.

Substituting Eq. (4) into Eq. (7), noting that $dE/dx \propto Z^2A/E$, and rearranging terms give us the expression

$$E = Z^2A(k')^{1/n'}\left(\frac{1}{\cot\theta - 1}\right)^{1/n'}. \tag{8}$$

So, if tracks become undetectable at some track angle $\theta_{\max}$, the corresponding upper energy bound $E_{\max}$ is proportional to $Z^2A(k')^{1/n'}$. This means that larger mass particles have a higher max energy beyond which they cannot be detected. This also shows that the exact bound is somewhat dependent on the CR-39 properties themselves, meaning that some variation would exist between different pieces.

The lower energy bound is more difficult to ascertain analytically due to $\vec{v}_T$ changing dramatically through the depth of the track and dE/dx's complicated Z dependence.

V. EXPERIMENTAL MEASUREMENTS OF ION TRACK PROPERTIES

Previous data have been published on the diameter–energy relationship for protons in CR-39,[27] but little research has been performed to demonstrate that other particles follow these models. Additionally, no recent data exist for the energy range of any particles in CR-39, which is thought to be sensitive to the exact manufacturing process of the CR-39. It is not clear whether or not these processes have remained consistent over the decades. In

this section, we will present data from TasTrak® CR-39[41] for protons, deuterons, and tritons, first showing CPS measurements of the knock-on deuterons and tritons from Eqs. (2a) and (2b) and then WRF measurements of the T^3He deuterons from Eq. (1), as well as D^3He protons. Various etch times between 2 h and 5 h are shown to represent typical data conditions.

A. Deuteron and triton measurements with CPS

CPS is used to measure charged particle spectra. This system has a calibrated magnet that deflects particles onto a CR-39 detector. The exact position on the detector is determined by the deflection angle, which is a monotonic function of the particle's energy.

We can use CPS to determine the energy–diameter relationship of CR-39 since particle's energies are uniquely determined by their position on the detector. The diameters themselves are not used in the CPS spectral analysis, so no independent measure of the source energy is required, making CPS ideal for this study.

In any DT implosion, some fraction of the DT neutrons will produce high energy "knock-on" deuterons and tritons that are emitted from the implosion in accordance with Eqs. (2a) and (2b).[5] These spectra are ideal for assessing the CR-39 diameter–energy relationships because they both are continuous over a wide range of energies.

Additionally, we can investigate the energy range using these spectra by looking at the track contrast as a function of particle energy. In this scope, track contrast is defined as the brightness of the darkest pixel within a track divided by the mean brightness of the frame that contains it. By this definition, low values of contrast are dark and easily detectable, while high values are faint. In practice, anything with values below 35% contrast is fully detectable and functional in analyses. Figure 6 shows an example of a CPS2 measurement from the OMEGA Laser Facility.[42]

Figure 6 shows that both the c-parameter model and the two-parameter model are able to well describe the deuteron and triton energy–diameter relationships. This is in agreement with the

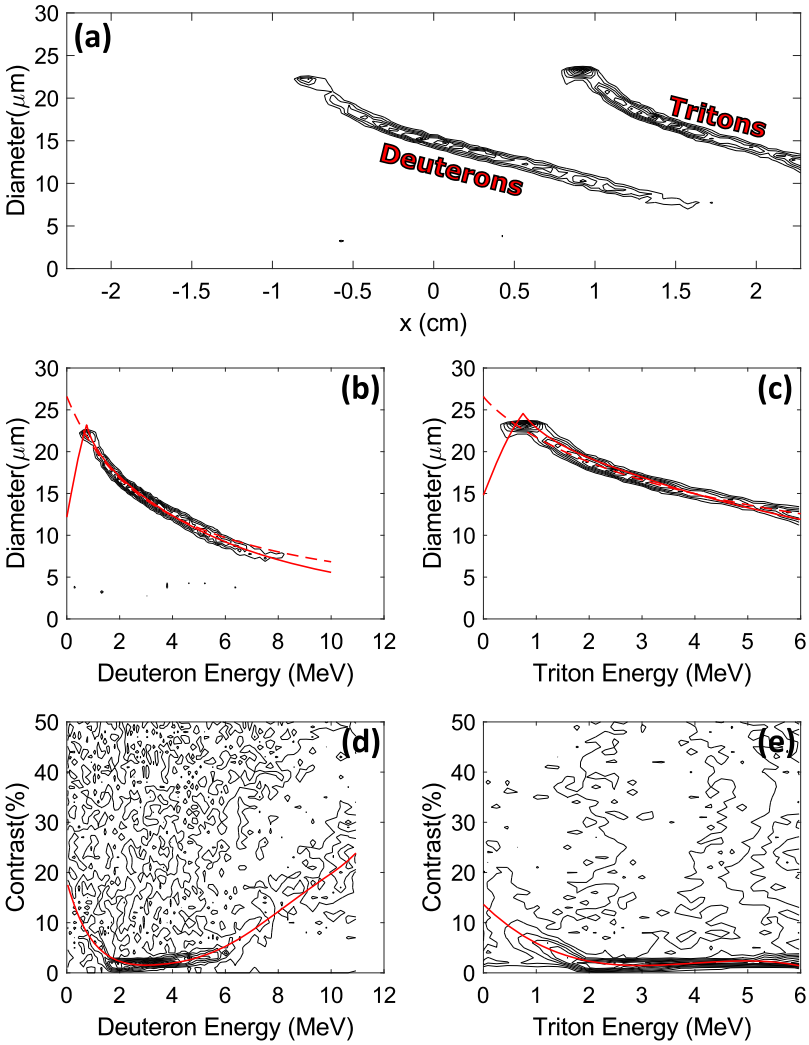

FIG. 6. Example CPS data from OMEGA shot 85 490. Figure 6(a) shows the raw diameter-vs-position contour plots for the knock-on deuterons and tritons. Figures 6(b) and 6(c) show the data re-binned with respect to the energies on the detector for the knock-on deuterons and knock-on tritons, respectively. Figures 6(d) and 6(e) are contour plots of energy vs track contrast for the deuteron and triton data, respectively. Note that contrast is defined in such a way that low values are dark and easily detectable, while high values are faint. In Figs. 6(a), 6(b), and 6(c), the contour levels vary from 20% to 100% of the maximum value. In Figs. 6(d) and 6(e), the contour levels vary from 0% to 100% of the maximum value. The solid red curve in Figs. 6(b) and 6(c) are the best fits using the c-parameter model. They use c parameters of 0.625 and 0.485 and have max diameters of 22.5 μm and 23.5 μm, respectively. Similarly, the dotted red curve is the best fits using the two-parameter model. They use k' values of 0.581 and 0.418 and n' values of 0.997 and 0.894, respectively. The solid red curve in Figs. 6(d) and 6(e) traces the maximum contour as a function of energy. The data shown here were etched for τ_E = 5.0 h.

simulation results discussed in Sec. III. Also in agreement is the fact that a low c parameter (<1) is required to describe the deuteron data and an even lower value is needed to describe the triton data. The fit values from other data are provided in Table II to demonstrate the consistency of this observation.

Data shown in Fig. 6 also suggest that the entire knock-on deuteron and triton spectra (when ranged through 25 μm of Al) fall below the 35% detectable contrast threshold. Specifically, these measurements confirm that the upper energy bound for 100% detection efficiency is at least 12.2 MeV for deuterons and 10 MeV for tritons. Note that the scaling derived in Eq. (8) suggests that the upper energy bound for tritons would be well beyond 10 MeV.

A lower energy bound can also be established from the data presented in Table II. The energy at which the max diameter occurs is in the lower energy regime of rapid track contrast fading. This can be visualized by comparing Figs. 6(b) and 6(c) with Figs. 6(d) and 6(e). Beyond this point, tracks are rapidly fading or already undetectable, making it an excellent candidate for the lower energy bound.

The energies in Table II tend to increase with the etch time as would be expected due to the lower energy tracks being etched out by the bulk etch wave. They are also fairly consistent between deuterons and tritons, perhaps due to an inability to resolve the small differences predicted in Fig. 8. Finally, there are some notable variations from piece to piece that correlate with the c parameter, meaning that the actual bound is a function of the intrinsic properties of the CR-39. For this reason, a great deal of conservatism is recommended when designing around the lower energy limit of CR-39.

B. Deuteron and proton measurements with WRFs

The WRFs are used to measure charged particle spectra with a calibrated aluminum wedge filter ranging from ~100 μm s to ~2000 μm s in thickness.[5,12] Where the particles are detected spatially on the CR-39 relates to a particular aluminum thickness, which can ultimately be used to determine the spectrum.

For the purposes of this paper, the WRF data can also be used to extract the diameter–energy relationship for a particular particle. When exposed to a mono-energetic source, the CR-39 detector measures a continuum of energies between zero and some energy less than the original source. The track diameters vary with the spatial position behind the WRF, and if the source energy is known, the relationship between the energy and spatial position can be determined, giving a direct measurement of the diameter–energy relationship.

Several recent experiments at the NIF and OMEGA have used DT^{3}He gas fills with a large variety of different objectives. Some of these experiments fielded WRFs, which measured both the 14.7 MeV D^{3}He proton line and the 9.5 MeV T^{3}He deuteron line. An example of this is shown in Fig. 7.

Figure 7 shows that both the c-parameter model and the two-parameter model are able to well describe both the proton and deuteron data. Also in agreement is the fact that the c parameter that best describes the deuteron data is much lower than that of the c parameter that best describes protons while the two k' and n' values are more similar. A handful of other examples are listed in Table III that demonstrate the consistency of this observation.

The data in Table III also include the energy at which the max diameter occurs [$E(D_{max})$] for deuterons and protons and the energy at which tracks fade beyond a contrast of 35% ($E_{c=35\%}$) for protons. They serve as effective lower and upper energy bounds, respectively. The lower energy bound for deuterons is in fair agreement with the CPS data in Table II, and the upper energy bound is beyond what was measured by the WRFs (8 MeV). For protons, the lower energy bound is higher on average. The upper energy bound is well below

TABLE II. Diameter–energy model fit values to CPS2 knock-on deuteron and triton data. The data were obtained from different experiments and etched for 2 h, 4 h, and 5 h to investigate any changes with etch time. The two-parameter model shares similar fit values (k' and n') between the deuterons and tritons for a single piece of CR-39. This is because a majority of the changes in the diameter–energy model is captured by the ratio $E/(Z^2A)$. Antithetically, the c-parameter value is always smaller for tritons compared to deuterons to account for the mass differences. Both models have slight changes with etch time, specifically increases in the n' and c values. Finally, the energy at which the max diameter is found increases roughly linearly with etch time. This corresponds to lower energy tracks being etched away with an increased etch time.

		Deuterons					Tritons				
Shot	τ_E (h)	k'	n'	c	D_{max} (μm)	$E(D_{max})$ (MeV)	k'	n'	c	D_{max} (μm)	$E(D_{max})$ (MeV)
77 351	2.0	0.849	0.806	0.509	8.4 ± 0.5	0.48 ± 0.18	0.914	0.746	0.434	9.0 ± 0.5	0.36 ± 0.18
77 351	4.0	0.866	1.004	0.688	16.0 ± 0.5	0.76 ± 0.10	0.949	0.943	0.558	17.0 ± 0.5	0.75 ± 0.12
77 351	5.0	0.923	1.090	0.795	20.0 ± 0.5	0.78 ± 0.08	1.038	1.077	0.643	21.0 ± 0.5	0.87 ± 0.09
85 485	2.0	0.626	0.867	0.512	9.5 ± 0.5	0.30 ± 0.18	0.674	0.836	0.417	9.9 ± 0.5	0.21 ± 0.21
85 485	4.0	0.610	1.090	0.684	18.5 ± 0.5	0.56 ± 0.10	0.690	0.978	0.531	19.0 ± 0.5	0.51 ± 0.15
85 485	5.0	0.578	1.107	0.661	22.5 ± 0.5	0.72 ± 0.10	0.646	1.037	0.534	23.5 ± 0.5	0.66 ± 0.12
85 488	2.0	0.651	0.830	0.523	9.5 ± 0.5	0.26 ± 0.18	0.689	0.778	0.430	10.0 ± 0.5	0.15 ± 0.18
85 488	4.0	0.612	0.947	0.640	18.5 ± 0.5	0.46 ± 0.10	0.631	0.880	0.474	18.9 ± 0.5	0.48 ± 0.15
85 488	5.0	0.613	1.009	0.634	22.0 ± 0.5	0.70 ± 0.10	0.637	0.868	0.509	23.4 ± 0.5	0.51 ± 0.12
85 490	2.0	0.651	0.779	0.508	9.5 ± 0.5	0.24 ± 0.16	0.638	0.780	0.400	10.0 ± 0.5	0.18 ± 0.18
85 490	4.0	0.618	0.956	0.612	18.0 ± 0.5	0.56 ± 0.12	0.621	0.881	0.471	19.0 ± 0.5	0.48 ± 0.15
85 490	5.0	0.583	0.990	0.628	22.5 ± 0.5	0.62 ± 0.10	0.599	0.891	0.483	23.5 ± 0.5	0.57 ± 0.12

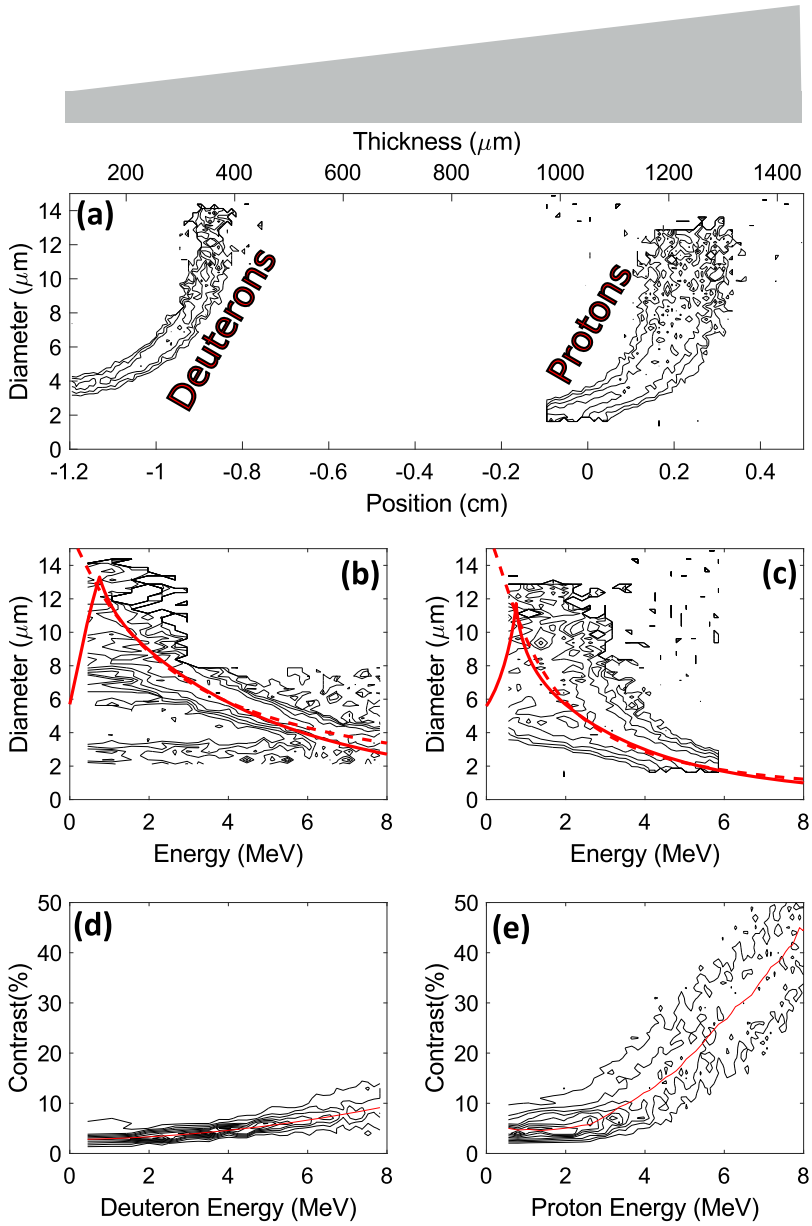

FIG. 7. Example WRF data from OMEGA shot 92 968. Figure 7(a) shows the raw track density contours binned with respect to their positions on the detector (with corresponding Al thicknesses) and track diameters. Figures 7(b) and 7(c) show the data re-binned with respect to the energies on the detector for the T^3He deuterons and D^3He protons, respectively. Figures 7(d) and 7(e) are contour plots of energy vs track contrast for the deuterons and protons, respectively. The solid red curves in Figs. 7(b) and 7(c) are the best fits using the c-parameter model. They use c parameters of 0.878 and 1.310, respectively. Similarly, the dashed red curves are the best fits using the two-parameter model. They use k' values of 0.809 and 0.655, respectively, and n' values of 1.103 and 1.403, respectively. The deuteron and proton lines were 9.547 MeV and 14.673 MeV, respectively, as measured by CPS2. For visualization, the contours plots in Figs. 7(a), 7(b), and 7(c) are normalized such that the integral over energy is constant for any diameter. The data shown here were etched for τ_E = 3.0 h.

TABLE III. Diameter–energy model fit values to WRF T^3He deuteron and D^3He proton data. The data were taken from different experiments and etched for either 2 h or 3 h. The c-parameter value is always smaller for deuterons compared to protons to account for the mass differences. Also listed are the energies at which the max diameter occurs [$E(D_{max})$] for the deuterons and protons and the energy at which tracks fade above 35% contrast ($E_{c=35\%}$) for protons. The WRFs did not measure deuterons below 8 MeV, which is well below their fading point.

		Deuterons					Protons					
Shot	τ_E (h)	k'	n'	c	D_{max} (μm)	$E(D_{max})$ (MeV)	k'	n'	c	D_{max} (μm)	$E(D_{max})$ (MeV)	$E_{c=35\%}$ (MeV)
92 966	2.0	0.868	1.322	0.827	9.2 ± 0.5	0.56 ± 0.10	0.625	1.594	1.324	8.8 ± 0.5	1.02 ± 0.56	4.3
92 968	3.0	0.809	1.103	0.878	14.3 ± 0.5	0.36 ± 0.06	0.655	1.403	1.310	13.0 ± 0.5	0.96 ± 0.52	6.4
92 969	3.0	0.781	1.198	0.891	14.3 ± 0.5	0.42 ± 0.06	0.742	1.423	1.372	13.0 ± 0.5	0.88 ± 0.47	4.4
92 972	3.0	0.671	1.340	0.827	14.3 ± 0.5	0.56 ± 0.08	0.587	1.491	1.299	13.0 ± 0.5	1.08 ± 0.58	5.1

that of the deuterons as expected and is in moderate agreement with previous claims.[5] As mentioned earlier, a great deal of variability is observed for both of the energy bounds.

VI. CONCLUSIONS

In this paper, it is shown that the diameter–energy relationship of both deuterons and tritons can be well described by the well established c-parameter model currently used for protons. This implies that the current established analysis techniques of WRFs and SRFs can be readily applied to protons, deuterons, and tritons to reliably infer accurate spectra.

Additionally, it was shown that the c-parameter values that best describe deuteron and triton data are significantly lower than those that describe proton data. This is due to the c-parameter model having no factor to account for the different masses of these particles. Current analysis techniques could be improved by taking advantage of this knowledge. For example, if the particle species is known prior to the analysis, an appropriate c-parameter guess could be generated to match the species. A species' exact c-parameter will still vary between pieces of CR-39, but will generally be similar to the corresponding values shown in Tables II and III.

Through simulations, it was shown that the c-parameter model is not expected to capture the behavior of alpha particles very well. This is thought to be due to higher order charge scaling in the stopping power leading to a fundamental change in the shape of the diameter–energy relationship. Data are needed to verify this prediction and, perhaps, adjust the model, so that the behavior of $Z = 2$ particles can be properly captured.

The two-parameter model derived in this work also appears capable of matching all of the observed data presented within. Its flexibility also allows it to match the simulated alpha data that could not be captured by the c-parameter model. In practice, the two-parameter model is harder to work with due to potential uniqueness issues in the fitting. For this reason, it is recommended to use the c-parameter model in any analyses whenever possible.

Data presented in this work also established rough bounds for the energy range of CR-39. Tracks have contrast below 35% for energies in the range of 1 MeV–4 MeV for proton data etched between 2 h and 3 h. Deuteron and triton data etched between 2 h and 5 h fell below this contrast limit for energies between 1 MeV and 12.2 MeV and 1–10 MeV, respectively. Contrast fading was not observed for triton generated tracks, and an upper energy bound is expected to be well above the 10 MeV limit established here. These limits will significantly aid in filtering designs for all CR-39 based diagnostics.

ACKNOWLEDGMENTS

The authors sincerely thank the OMEGA operations staff who supported this work and Bob Frankel and Ernie Doeg for processing the CR-39. This study is based on the work supported by the Department of Energy, National Nuclear Security Administration, under Award No. DE-NA0003868, by the National Laser Users' Facility under Award No. DE-NA0003539, and by the LLE under Award No. 417532-G. This report was prepared as an account of work sponsored by an agency of the United States Government. Neither the United States Government nor any agency thereof, nor any of their employees, makes any warranty, expressd or implied, or assumes any legal liability or responsibility for the accuracy, completeness, or usefulness of any information, apparatus, product, or process disclosed or represents that its use would not infringe privately owned rights. Reference, herein, to any specific commercial product, process, or service by trade name, trademark, manufacturer, or otherwise does not necessarily constitute or imply its endorsement, recommendation, or favoring by the United States Government or any agency thereof. The views and opinions of authors expressed herein do not necessarily state or reflect those of the United States Government or any agency thereof.

APPENDIX A: TWO PARAMETER MODEL DERIVATION

The track morphology is ultimately the intersection of the etched volumes described by the bulk etch and track etch processes. If one assumes that $|\vec{v}_T|$ is constant and parallel to the surface normal for some etch time of τ_E, the radius R of any bulk etch sphere with origin h away from the initial CR-39 surface is given by

$$R = |\vec{v}_B|\tau_E - hf_E, \tag{A1}$$

where f_E is the etch ratio $|\vec{v}_B|/|\vec{v}_T|$. The intersection of this sphere and the new surface $|\vec{v}_B|\tau_E$ down from the initial surface is then a circle with radius

$$R_\perp(h) = \sqrt{(|\vec{v}_B|\tau_E - hf_E)^2 - (h - |\vec{v}_B|\tau_E)^2}. \tag{A2}$$

The physical radius is the maximum of this function that occurs at

$$\operatorname{argmax} R_\perp(h) = |\vec{v}_B|\tau_E \frac{1}{f_E + 1}. \tag{A3}$$

Evaluating Eq. (A2) at this height and multiplying by 2 gives the physical diameter

$$D = 2|\vec{v}_B|\tau_E \sqrt{\frac{1 - f_E}{1 + f_E}}. \tag{A4}$$

Taylor expanding Eq. (A4) about f_E and dropping all terms of the second order or higher give the more common form

$$D = 2|\vec{v}_B|\tau_E \left(1 - \frac{|\vec{v}_B|}{|\vec{v}_T|}\right). \tag{A5}$$

Combining Eq. (4) into Eq. (A5) gives

$$D = 2|\vec{v}_B|\tau_E \left(1 - \frac{1}{1 + k\left(\frac{dE}{dx}\frac{\text{keV}}{\mu\text{m}}\right)^n}\right), \tag{A6}$$

which simplifies to

$$D = 2|\vec{v}_B|\tau_E \left(\frac{1}{1 + \left[k\left(\frac{dE}{dx}\frac{\text{keV}}{\mu\text{m}}\right)^n\right]^{-1}}\right). \tag{A7}$$

Finally, as it was assumed that $|\vec{v}_T|$ is constant, the Coulomb logarithm in $\frac{dE}{dx}$ is also relatively constant. In this case, $\frac{dE}{dx} \propto Z^2A/E$, which means

$$D(E) \sim \frac{2\tau_E|\vec{v}_B|}{1 + k'\left(E_{\mathrm{MeV}}/Z^2A\right)^{n'}}. \tag{A8}$$

APPENDIX B: c-PARAMETER MODEL

The c-parameter model is an empirical diameter–energy relationship that depends on one parameter c, as well as the measured parameter $D_{\max}$. It has been created to match a variety of observed proton data over decades of CR-39 use. These equations are more practical than the two-parameter model for fitting to data due to the reduction in free parameters. The c-parameter model is given by the following equations:

$$D(E) = \sum_{i=1}^{3} \alpha_i \exp\left[-\frac{E-1}{\beta_i}\right], \tag{B1}$$

i	α_i	β_i
1	1.2	0.3
2	11.3	3.0
3	4.8	8.0

$$D_c = \begin{cases} 20\exp(-c|\log(D/20)|) & D \le 20, \\ 40 - 20\exp(-c|\log(D/20)|) & D > 20, \end{cases} \tag{B2}$$

$$D_c = \begin{cases} \frac{(20-D)^2}{20-2D}\left[e^{\frac{c}{2}\log\left[\frac{D^2}{(20-D)^2}\right]} - 1\right] + 20 & D \le 10, \\ 20 - c(20-D) & D \ge 10, \end{cases} \tag{B3}$$

$$D(D_{\mathrm{raw}}, D_{\max}) = 20\left(\frac{D_{\mathrm{raw}}}{D_{\max}}\right)\left(\frac{1}{1 - MD_{\mathrm{raw}}}\right), \tag{B4}$$

$$M = \frac{20 - D_{\max}}{20D_{\max}}\left[\frac{7}{10}\left(1 - \frac{D_{\max}}{23}\right)(1-f) + \frac{f}{4}\right], \tag{B5}$$

$$f = \begin{cases} 0 & D_{\max} < 12.5, \\ \frac{D_{\max}-12.5}{20-12.5} & 12.5 \le D_{\max} \le 20, \\ 1 & D_{\max} > 20. \end{cases} \tag{B6}$$

APPENDIX C: MAX DIAMETER DISCUSSION

The c-parameter model depends on the parameter $D_{\max}$ in addition to the parameter c. $D_{\max}$ is a physically motivated metric that is supposed to be the largest significant diameter observed in the analysis. Including this parameter plays the role of accounting for τ_E, which is explicitly included in the two-parameter model. However, there are several examples of data where the observed $D_{\max}$ varies substantially for the same etch times. These are thought to be due to variations in $|\vec{v}_B|$ caused either by x-ray exposure[23,24] or variations in etching conditions.

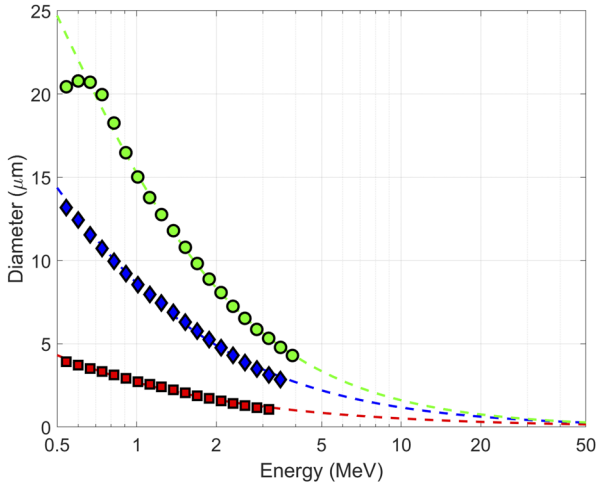

FIG. 8. Two-parameter model fits to simulated proton data. Simulated data are shown as red squares, blue diamonds, and green circles for simulated etch times of 1 h, 3 h, and 5 h, respectively. The two-parameter fit was performed using an etch time of 10 h to demonstrate the flexibility of the model when the etch time is completely unknown. These fits are shows as red, blue, and green dotted lines for the 1 h, 3 h, and 5 h data, respectively. All of the data are generated using $|\vec{v}_B| = 2.66$ μm/h, $\tau_E = 5$ h, $k = 6 \times 10^{-5}$, and $n = 2.76$ from Eq. (4) to resemble typical experimental data. The fits in both Figs. 1(a) and 1(b) use fit values shown in Table IV.

In comparison, the two-parameter model has no such physically motivated correction factor. The max diameter in that formulation ($2|\vec{v}_B|\tau_E$) is often 30% larger than any diameter that might be observed due to the assumptions used to derive the model. Variations in $|\vec{v}_B|$ cannot be accurately measured, so there is no way to truly account for it as the c-parameter model does. However, the increased flexibility of having two parameters enables fitting data even when the etch time is unknown. In Fig. 8, this is demonstrated by fitting simulated data using an incorrect value for τ_E.

Figure 8 shows that the two-parameter model can excellently match the simulated data even when using an etch time 10 times higher than that simulated. This means that any small variations $|\vec{v}_B|\tau_E$ can easily be accounted for without the need for an additional physical measurement. The fit values and their corresponding χ^2 values are shown in Table IV.

TABLE IV. Two-parameter fit values for various simulated and assumed etch times.

τ_E simulated (h)	τ_E assumed (h)	k'	n'	χ^2
1.0	1.0	0.894	1.343	0.0206
3.0	3.0	0.829	1.413	0.0701
5.0	5.0	0.769	1.467	0.1981
1.0	10.0	18.82	0.734	0.2039
3.0	10.0	5.156	0.933	0.1493
5.0	10.0	2.489	1.110	0.0269

APPENDIX D: COMPARISON OF MODELS

It has been shown that both the c-parameter model and the two-parameter model are able to match data for protons, deuterons, and tritons. A natural question to ask is how well the two models match one another. The two-parameter model is more flexible as demonstrated by its ability to fit simulated alpha data in Fig. 4(a), so the c-parameter model can be thought of as a special case of the two parameter model. They both cannot match perfectly as one is a power-law while the other is governed by exponentials, but their behavior is quite similar. A detailed comparison of them for various parameters is shown in Fig. 9.

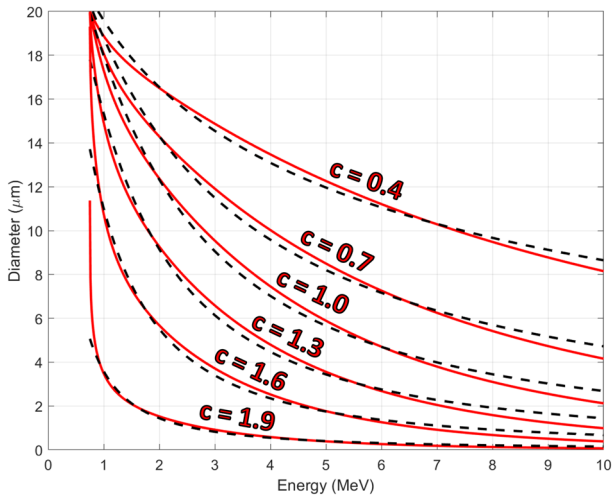

FIG. 9. Comparison between the c-parameter model (solid red curves) and the two-parameter model (black dashed curves). The two-parameter model parameters are chosen to best-fit various c parameters. Models do not perfectly match but never deviate beyond 1 μm of one another.

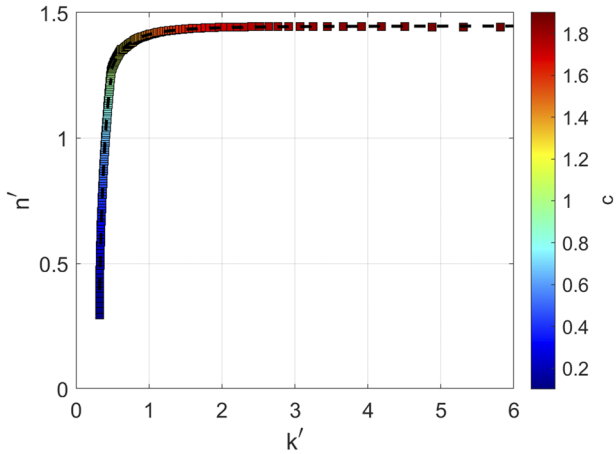

FIG. 10. Best fit k' and n' values to the c-parameter model for various c parameters. Data point locations represent the best fit values, while the color of the data point represents the corresponding c parameter. The black dashed curve is an empirical power-law fit to the relation between k' and n'.

The two-parameter model can be reduced to a single parameter if the model is restricted to the family of curves that best fit the c-parameter model. Performing this not only removes uniqueness concerns but also eliminates the two-parameters model's ability to fit to simulated alpha data. The relation between k' and n' for this restricted set of curves is shown in Fig. 10. The empirical fit to this relation is

$$n' = \begin{cases} 1.468 - 0.01376(k')^{-3.847} & k < 0.4807, \\ 1.447 - 0.03441(k')^{-2.233} & k \geq 0.4807. \end{cases} \quad \text{(D1)}$$

REFERENCES

[1]S. Kacenjar, L. Goldman, and A. Entenberg, Rev. Sci. Instrum. **52**, 831 (1981).
[2]S. Kacenjar, S. Skupsky, A. Entenberg, L. Goldman, and M. Richardson, Phys. Rev. Lett. **49**, 463 (1982).
[3]R. J. Leeper, J. R. Lee, L. Kissel, D. J. Johnson, W. A. Stygar, and D. E. Hebron, J. Appl. Phys. **60**, 4059 (1986).
[4]J. A. Frenje, C. K. Li, F. H. Séguin, D. G. Hicks, S. Kurebayashi, R. D. Petrasso, S. Roberts, V. Y. Glebov, D. D. Meyerhofer, T. C. Sangster, J. M. Soures, C. Stoeckl, C. Chiritescu, G. J. Schmid, and R. A. Lerche, Rev. Sci. Instrum. **73**, 2597 (2002).
[5]F. H. Séguin, J. A. Frenje, C. K. Li, D. G. Hicks, S. Kurebayashi, J. R. Rygg, B.-E. Schwartz, R. D. Petrasso, S. Roberts, J. M. Soures, D. D. Meyerhofer, T. C. Sangster, J. P. Knauer, C. Sorce, V. Y. Glebov, C. Stoeckl, T. W. Phillips, R. J. Leeper, K. Fletcher, and S. Padalino, Rev. Sci. Instrum. **74**, 975 (2003).
[6]F. H. Séguin, J. L. DeCiantis, J. A. Frenje, S. Kurebayashi, C. K. Li, J. R. Rygg, C. Chen, V. Berube, B. E. Schwartz, R. D. Petrasso, V. A. Smalyuk, F. J. Marshall, J. P. Knauer, J. A. Delettrez, P. W. McKenty, D. D. Meyerhofer, S. Roberts, T. C. Sangster, K. Mikaelian, and H. S. Park, Rev. Sci. Instrum. **75**, 3520 (2004).
[7]J. L. DeCiantis, F. H. Séguin, J. A. Frenje, V. Berube, M. J. Canavan, C. D. Chen, S. Kurebayashi, C. K. Li, J. R. Rygg, B. E. Schwartz, R. D. Petrasso, J. A. Delettrez, S. P. Regan, V. A. Smalyuk, J. P. Knauer, F. J. Marshall, D. D. Meyerhofer, S. Roberts, T. C. Sangster, C. Stoeckl, K. Mikaelian, H. S. Park, and H. F. Robey, Rev. Sci. Instrum. **77**, 043503 (2006).
[8]J. A. Frenje, D. T. Casey, C. K. Li, J. R. Rygg, F. H. Séguin, R. D. Petrasso, V. Y. Glebov, D. D. Meyerhofer, T. C. Sangster, S. Hatchett, S. Haan, C. Cerjan, O. Landen, M. Moran, P. Song, D. C. Wilson, and R. J. Leeper, Rev. Sci. Instrum. **79**, 10E502 (2008).
[9]C. G. Freeman, G. Fiksel, C. Stoeckl, N. Sinenian, M. J. Canfield, G. B. Graeper, A. T. Lombardo, C. R. Stillman, S. J. Padalino, C. Mileham, T. C. Sangster, and J. A. Frenje, Rev. Sci. Instrum. **82**, 073301 (2011).
[10]A. B. Zylstra, C. K. Li, H. G. Rinderknecht, F. H. Séguin, R. D. Petrasso, C. Stoeckl, D. D. Meyerhofer, P. Nilson, T. C. Sangster, S. L. Pape, A. Mackinnon, and P. Patel, Rev. Sci. Instrum. **83**, 013511 (2012).
[11]A. B. Zylstra, J. A. Frenje, F. H. Séguin, M. J. Rosenberg, H. G. Rinderknecht, M. G. Johnson, D. T. Casey, N. Sinenian, M. J.-E. Manuel, C. J. Waugh, H. W. Sio, C. K. Li, R. D. Petrasso, S. Friedrich, K. Knittel, R. Bionta, M. McKernan, D. Callahan, G. W. Collins, E. Dewald, T. Döppner, M. J. Edwards, S. Glenzer, D. G. Hicks, O. L. Landen, R. London, A. Mackinnon, N. Meezan, R. R. Prasad, J. Ralph, M. Richardson, J. R. Rygg, S. Sepke, S. Weber, R. Zacharias, E. Moses, J. Kilkenny, A. Nikroo, T. C. Sangster, V. Glebov, C. Stoeckl, R. Olson, R. J. Leeper, J. Kline, G. Kyrala, and D. Wilson, Rev. Sci. Instrum. **83**, 10D901 (2012).
[12]F. H. Seguin, N. Sinenian, M. Rosenberg, A. Zylstra, M. J.-E. Manuel, H. Sio, C. Waugh, H. G. Rinderknecht, M. G. Johnson, J. Frenje, C. K. Li, R. Petrasso, T. C. Sangster, and S. Roberts, Rev. Sci. Instrum. **83**, 10D908 (2012).
[13]D. T. Casey, J. A. Frenje, M. G. Johnson, F. H. Séguin, C. K. Li, R. D. Petrasso, V. Y. Glebov, J. Katz, J. P. Knauer, D. D. Meyerhofer, T. C. Sangster, R. M. Bionta, D. L. Bleuel, T. Döppner, S. Glenzer, E. Hartouni, S. P. Hatchett, S. L. Pape, T. Ma,

A. MacKinnon, M. A. Mckernan, M. Moran, E. Moses, H.-S. Park, J. Ralph, B. A. Remington, V. Smalyuk, C. B. Yeamans, J. Kline, G. Kyrala, G. A. Chandler, R. J. Leeper, C. L. Ruiz, G. W. Cooper, A. J. Nelson, K. Fletcher, J. Kilkenny, M. Farrell, D. Jasion, and R. Paguio, Rev. Sci. Instrum. **83**, 10D912 (2012).

[14]D. T. Casey, J. A. Frenje, M. G. Johnson, F. H. Séguin, C. K. Li, R. D. Petrasso, V. Y. Glebov, J. Katz, J. Magoon, D. D. Meyerhofer, T. C. Sangster, M. Shoup, J. Ulreich, R. C. Ashabranner, R. M. Bionta, A. C. Carpenter, B. Felker, H. Y. Khater, S. LePape, A. MacKinnon, M. A. McKernan, M. Moran, J. R. Rygg, M. F. Yeoman, R. Zacharias, R. J. Leeper, K. Fletcher, M. Farrell, D. Jasion, J. Kilkenny, and R. Paguio, Rev. Sci. Instrum. **84**, 043506 (2013).

[15]A. B. Zylstra, M. G. Johnson, J. A. Frenje, F. H. Séguin, H. G. Rinderknecht, M. J. Rosenberg, H. W. Sio, C. K. Li, R. D. Petrasso, M. McCluskey, D. Mastrosimone, V. Y. Glebov, C. Forrest, C. Stoeckl, and T. C. Sangster, Rev. Sci. Instrum. **85**, 063502 (2014).

[16]M. G. Johnson, J. A. Frenje, C. K. Li, F. H. Séguin, R. D. Petrasso, R. M. Bionta, D. T. Casey, J. A. Caggiano, R. Hatarik, H. Y. Khater, D. B. Sayre, J. P. Knauer, T. C. Sangster, H. W. Herrmann, and J. D. Kilkenny, Rev. Sci. Instrum. **85**, 11E104 (2014).

[17]M. J. Rosenberg, A. B. Zylstra, J. A. Frenje, H. G. Rinderknecht, M. G. Johnson, C. J. Waugh, F. H. Séguin, H. Sio, N. Sinenian, C. K. Li, R. D. Petrasso, V. Y. Glebov, M. Hohenberger, C. Stoeckl, T. C. Sangster, C. B. Yeamans, S. LePape, A. J. Mackinnon, R. M. Bionta, B. Talison, D. T. Casey, O. L. Landen, M. J. Moran, R. A. Zacharias, J. D. Kilkenny, and A. Nikroo, Rev. Sci. Instrum. **85**, 103504 (2014).

[18]C. J. Waugh, M. J. Rosenberg, A. B. Zylstra, J. A. Frenje, F. H. Séguin, R. D. Petrasso, V. Y. Glebov, T. C. Sangster, and C. Stoeckl, Rev. Sci. Instrum. **86**, 053506 (2015).

[19]A. B. Zylstra, H.-S. Park, J. S. Ross, F. Fiuza, J. A. Frenje, D. P. Higginson, C. Huntington, C. K. Li, R. D. Petrasso, B. Pollock, B. Remington, H. G. Rinderknecht, D. Ryutov, F. H. Séguin, D. Turnbull, and S. C. Wilks, Rev. Sci. Instrum. **87**, 11E704 (2016).

[20]M. G. Johnson, J. A. Frenje, R. M. Bionta, D. T. Casey, M. J. Eckart, M. P. Farrell, G. P. Grim, E. P. Hartouni, R. Hatarik, M. Hoppe, J. D. Kilkenny, C. K. Li, R. D. Petrasso, H. G. Reynolds, D. B. Sayre, M. E. Schoff, F. H. Séguin, K. Skulina, and C. B. Yeamans, Rev. Sci. Instrum. **87**, 11D816 (2016).

[21]M. G. Johnson, J. Katz, C. Forrest, J. A. Frenje, V. Y. Glebov, C. K. Li, R. Paguio, C. E. Parker, C. Robillard, T. C. Sangster, M. Schoff, F. H. Seguin, C. Stoeckl, and R. D. Petrasso, Rev. Sci. Instrum. **89**, 10I129 (2018).

[22]D. J. Ampleford, C. L. Ruiz, D. N. Fittinghoff, J. D. Vaughan, K. Hahn, B. Lahmann, M. Gatu-Johnson, J. Frenje, R. Petrasso, C. R. Ball, A. J. Maurer, P. F. Knapp, A. J. Harvey-Thompson, J. Fisher, P. Alberto, J. A. Torres, G. Cooper, B. Jones, G. A. Rochau, and M. J. May, Rev. Sci. Instrum. **89**, 10I132 (2018).

[23]H. G. Rinderknecht, J. Rojas-Herrera, A. B. Zylstra, J. A. Frenje, M. G. Johnson, H. Sio, N. Sinenian, M. J. Rosenberg, C. K. Li, F. H. Séguin, R. D. Petrasso, T. Filkins, J. A. Steidle, J. A. Steidle, N. Traynor, and C. Freeman, Rev. Sci. Instrum. **86**, 123511 (2015).

[24]J. Rojas-Herrera, H. G. Rinderknecht, A. B. Zylstra, M. G. Johnson, D. Orozco, M. J. Rosenberg, H. Sio, F. H. Seguin, J. A. Frenje, C. K. Li, and R. D. Petrasso, Rev. Sci. Instrum. **86**, 033501 (2015).

[25]R. O. Stapf, H. Azechi, N. Miyanaga, H. Nakaishi, M. Yamanaka, Y. Izawa, T. Yamanaka, and C. Yamanaka, Nucl. Instrum. Methods Phys. Res., Sect. A **254**, 135 (1987).

[26]K. Oda, M. Ito, H. Miyake, M. Michijima, and J. Yamamoto, Nucl. Instrum. Methods Phys. Res., Sect. B **35**, 50 (1988).

[27]N. Sinenian, M. J. Rosenberg, M. Manuel, S. C. McDuffee, D. T. Casey, A. B. Zylstra, H. G. Rinderknecht, M. G. Johnson, F. H. Séguin, J. A. Frenje, C. K. Li, and R. D. Petrasso, Rev. Sci. Instrum. **82**, 103303 (2011).

[28]M. J. Rosenberg, F. H. Séguin, C. J. Waugh, H. G. Rinderknecht, D. Orozco, J. A. Frenje, M. G. Johnson, H. Sio, A. B. Zylstra, N. Sinenian, C. K. Li, R. D. Petrasso, V. Y. Glebov, C. Stoeckl, M. Hohenberger, T. C. Sangster, S. LePape, A. J. Mackinnon, R. M. Bionta, O. L. Landen, R. A. Zacharias, Y. Kim, H. W. Herrmann, and J. D. Kilkenny, Rev. Sci. Instrum. **85**, 043302 (2014).

[29]A. B. Zylstra, H. W. Herrmann, M. G. Johnson, Y. H. Kim, J. A. Frenje, G. Hale, C. K. Li, M. Rubery, M. Paris, A. Bacher, C. R. Brune, C. Forrest, V. Y. Glebov, R. Janezic, D. McNabb, A. Nikroo, J. Pino, T. C. Sangster, F. H. Séguin, W. Seka, H. Sio, C. Stoeckl, and R. D. Petrasso, Phys. Rev. Lett. **117**, 035002 (2016).

[30]A. B. Zylstra, H. W. Herrmann, M. G. Johnson, Y. H. Kim, J. A. Frenje, G. Hale, C. K. Li, M. Rubery, M. Paris, A. Bacher, C. R. Brune, C. Forrest, V. Y. Glebov, R. Janezic, D. McNabb, A. Nikroo, J. Pino, T. C. Sangster, F. H. Séguin, W. Seka, H. Sio, C. Stoeckl, and R. D. Petrasso, Phys. Rev. Lett. **119**, 222701 (2017).

[31]M. G. Johnson, D. T. Casey, M. Hohenberger, A. B. Zylstra, A. Bacher, C. R. Brune, R. M. Bionta, R. S. Craxton, C. L. Ellison, M. Farrell, J. A. Frenje, W. Garbett, E. M. Garcia, G. P. Grim, E. Hartouni, R. Hatarik, H. W. Herrmann, M. Hohensee, D. M. Holunga, M. Hoppe, M. Jackson, N. Kabadi, S. F. Khan, J. D. Kilkenny, T. R. Kohut, B. Lahmann, H. P. Le, C. K. Li, L. Masse, P. W. McKenty, D. P. McNabb, A. Nikroo, T. G. Parham, C. E. Parker, R. D. Petrasso, J. Pino, B. Remington, N. G. Rice, H. G. Rinderknecht, M. J. Rosenberg, J. Sanchez, D. B. Sayre, M. E. Schoff, C. M. Shuldberg, F. H. Seguin, H. Sio, Z. B. Walters, and H. D. Whitley, Phys. Plasmas **25**, 056303 (2018).

[32]G. Sutcliffe, "A new tri-particle backlighter and stopping power platform for high-energy-density plasmas" (unpublished).

[33]C. K. Li, F. H. Séguin, D. G. Hicks, J. A. Frenje, K. M. Green, S. Kurebayashi, R. D. Petrasso, D. D. Meyerhofer, J. M. Soures, V. Y. Glebov, R. L. Keck, P. B. Radha, S. Roberts, W. Seka, S. Skupsky, C. Stoeckl, and T. C. Sangster, Phys. Plasmas **8**, 4902 (2001).

[34]S. Durrani and R. K. Bull, *Solid State Nuclear Track Detection Principles, Methods and Applications* (Pergamon Book Ltd., 1987).

[35]H. Bethe and J. Ashkin, *Experimental Nuclear Physics* (Wiley, 1953) p. 253.

[36]J. F. Ziegler, J. P. Biersack, and M. D. Ziegler, *The Stopping and Range of Ions in Matter* (SRIM Company, 2015).

[37]V. F. Bloch, Ann. Phys. **408**, 285 (1933).

[38]C.-M. C. Ma and T. Lomax, *Proton and Carbon Ion Therapy* (CRC Press, 2012).

[39]N. Sinenian, M. J.-E. Manuel, A. B. Zylstra, M. Rosenberg, C. J. Waugh, H. G. Rinderknecht, D. T. Casey, H. Sio, J. K. Ruszczynski, L. Zhou, M. G. Johnson, J. A. Frenje, F. H. Séguin, C. K. Li, R. D. Petrasso, C. L. Ruiz, and R. J. Leeper, Rev. Sci. Instrum. **83**, 043502 (2012).

[40]D. G. Hicks, "Charged-particle spectroscopy: A new window on inertial confinement fusion, Ph.D. thesis, Massachusetts Institute of Technology, 1999.

[41]T. A. S. Ltd., TASTRAC PADC, 2015, http://www.tasl.co.uk/plastics.php.

[42]T. R. Boehly, D. L. Brown, R. S. Craxton, R. L. Keck, J. P. Knauer, J. H. Kelly, T. J. Kessler, S. A. Kumpan, S. J. Loucks, S. A. Letzring, F. J. Marshall, R. L. McCrory, S. F. B. Morse, W. Seka, J. M. Soures, and C. P. Verdon, Opt. Commun. **133**, 495 (1997).